

Development of a miniature Doppler lidar for velocity measurements of small particles and droplets

Jan Kai Bohrer

von Karman Institute for Fluid Dynamics, Environmental and Applied Fluid Dynamics

(Dated: 30th of June, 2022)

Building a so far commercially unavailable, compact, lightweight and robust Doppler lidar design would enable various possibilities, including non-intrusive wind tunnel measurements and drone mounted applications. Additionally, the probe volume of conventional lidars can be reduced by decreasing the measurement distance to a few meters and by the use of a bistatic setup. This work presents the development of a bistatic lidar, using a visible, continuous wave HeNe laser and its two-stage validation by measuring the velocity of a flywheel target with adjustable rotation speed and by particle tracking velocimetry (PTV) of water droplets in an open wind tunnel stream. The lidar is successfully validated by the flywheel in the velocity range from 0.5 to 7.5 m/s. The lidar is also able to measure the velocity of wind tunnel driven droplets of 2 mm diameter in a droplet velocity range of 0.2 to 0.4 m/s. Although the fluctuations of droplet trajectories in the unsteady wind tunnel stream lead to significant measurement uncertainties, the validation by PTV still remains conclusive. The lidar proves to be unable to measure the speed of a spray of water droplets, generated by a vaporizer, due to insufficient laser intensity. The work concludes with recommendations for the improvement of the developed lidar.

I. INTRODUCTION

Light detection and ranging (lidar) is an optical remote sensing technology for the measurement of atmospheric and/or surface properties. A laser beam is targeted at a surface or volume of interest. After scattering from the target region, the returning light is collected by a receiver element. By analyzing the relation of received and emitted light characteristics, a variety of properties can be determined, based on the technology specifications. Different lidar types have been developed to measure, among others, point to point distances, surface vibration characteristics, atmospheric density and temperature profiles, aerosol size distribution, chemical composition and flow velocities. Applications of the technology include topographic elevation mapping, short term turbulence predictions in airplanes, atmospheric wind profile determination and weather forecasting. [1]

The presented work focuses on the lidar based measurement of wind velocity fields. State of the art short range lidars are able to scan the atmosphere and generate velocity profiles from about 10 to 200 meters [2]. Another application is to mount the lidar on airplanes or on the nacelles of wind turbines to scan the surrounding velocity field to optimize operation and analyze influence of turbine wakes. These lidar applications are sophisticated, commonly used on industrial scale and able to supply reliable information about the surrounding wind field. One big shortcoming is the large size and weight of the lidars, which makes them hard to move and limits them to stationary application. Moreover, the minimum

measurement range is limited, i.e., regions which are too close to the lidars can not be investigated. In the era of emerging unmanned aerial vehicle remote monitoring of wind turbines and other technical structures, the demand for lightweight and compact optical sensors is rising [3, 4].

Additionally, lidar velocimetry in wind tunnels can provide significant advantages over other measurement techniques, including non-intrusive measurements, remote and flexible application, low laser intensity requirements and applicability without flow seeding. Nevertheless, there were only a few recent attempts for the adaptation of Doppler lidars for wind tunnels [5–8]. Although the results for the velocity field are promising, the application is limited, because of the relative size of lidar and wind tunnel and the minimum measurement distance of about 10 m [4, 9]. Either the big lidars need to be placed outside of the wind tunnel or the wind tunnel has to be very large, such that the apparatus does not influence the flow significantly [5, 7, 8].

The work of Barnhart [9] treats the development of a coherent lidar for wind tunnel measurements. In this work, the goal was to use Rayleigh scattering on air molecules to determine the Doppler signal. Lidars for wind energy applications usually depend on Mie scattering from natural abundant aerosols [10]. Indeed, it was not possible in [9] to achieve a measurable signal in the wind tunnel for unseeded flow with a 200 mW visible laser. Only when seeding the flow with water droplets, a sufficient signal-to-noise ratio could be achieved for the presented design.

Vasiljevic *et al.* [4] use the infrared lidar prototype ‘ZXT2’, built by ZX Lidars with a two-channel continuous wave laser rack, which can reach power values of 1.3 W. Applying 300 mW per laser, the authors report sufficient signal strength to measure aerosol velocities in the atmosphere. A proof of concept for a drone based application was successfully conducted. For this proof of concept, only the telescopes were mounted on the drone, while the laser and the rest of the lidar components remain on the ground. The connection was established via optical cables of 100 m length, which transmit the light information between the lidar base on the ground and the drone with transmitter and receiver lenses in the air. Not surprisingly, this introduces some major drawbacks, including instability and limitation of security due to the dangling cables.

It would thus be desirable to develop a compact, lightweight and robust lidar design which can fulfill two demands: Non-intrusive velocity measurement in wind tunnels and outdoor applications mounting the complete lidar setup on agile, maneuverable drones. On the other hand, the lidar should be as affordable as possible to compete with other measurement techniques and ground and nacelle mounted scanning lidars. The objectives of the presented work are to develop a lidar system with the provided resources, assess its capabilities and limitations and find ways to improve the setup. Two methods are applied for the lidar validation. First, a flywheel calibration, as described in [5, 11], where a solid disc turns with known angular velocity. Pointing the lidar under a flat angle onto the rotating rim simulates a target with constant line-of-sight (LOS) velocity. Second, high speed imaging and particle tracking velocimetry of water droplets in an open wind tunnel stream.

Section II describes the methodology of the lidar principle, the developed data processing algorithms and the two validation setups. In Sec. III, the results of the lidar validations are presented. The final Sec. IV draws conclusions and provides recommendations, how to improve the lidar setup.

II. METHODOLOGY

This section introduces the lidar working principle (Sec. II A) and general setup (Sec. II B), and presents the developed data processing algorithms (Sec. II C), the setups for lidar validation with a flywheel (Sec. II D) and the measurement procedure for droplets in an open wind tunnel stream, including validation by particle tracking velocimetry (Sec. II E).

A. Lidar principle

A Doppler lidar can be used to measure the line-of-sight (LOS) velocity of particles inside a probe volume, as illustrated in the general setup in Fig. 1 by [12]. Laser light is emitted with power P_T , wavelength $\lambda_0 = \lambda_{\text{vac}}/n_0$ and frequency $f_0 = c_0/\lambda_0$, by a transmitter and aimed on a region in space. Here, λ_{vac} is the wavelength in vacuum, n_0 is the refractive index of the medium (i.e. ambient air) and c_0 is the speed of light. Particles in the probe volume scatter part of the light backwards to the receiver, where it is analyzed. If the target particles have a velocity component v_{LOS} in the lidar line-of-sight direction, the frequency of the scattered light is Doppler-shifted to $f_s = f_0 + f_D$, where $f_D = -2v_{\text{LOS}}/\lambda_0$ is called Doppler shift. In coherent lidar systems, the original laser light is split into a reference beam, called ‘local oscillator’ (LO), and the transmission beam.

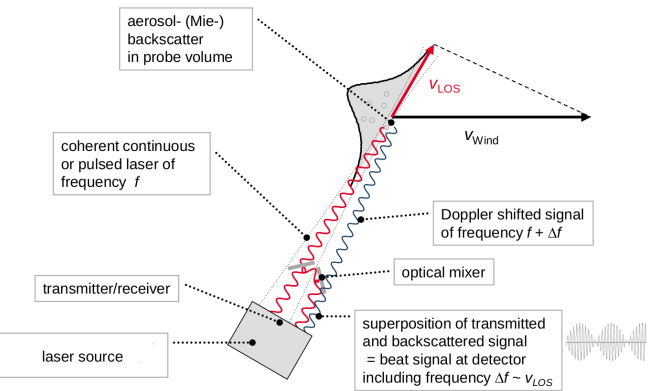


FIG. 1. General lidar principle and probe volume. Figure from [12].

The receiver collects light with power P_s and frequency f_s , which is mixed with the local oscillator with power P_{LO} and frequency f_{LO} . In the used setup, the local oscillator frequency f_{LO} is equal f_0 . It general it can however be modulated to enable sign determination of v_{LOS} . The mixed signal is focused on a photo detector (e.g. PIN diode or avalanche photo multiplier), which results in an output beat signal $I(t) \propto I_c + 2E_{\text{LO}}E_s \cos(2\pi(f_s - f_{\text{LO}})t - \phi_s)$, where I_c is a constant offset, and $E_s \propto \sqrt{P_s}$ and $E_{\text{LO}} \propto \sqrt{P_{\text{LO}}}$ are the electric field amplitudes. E_{LO} is usually larger than E_s . $I(t)$ oscillates with the frequency $f_D = f_s - f_{\text{LO}}$ and ϕ_s is the phase shift between signal and local oscillator [10].

The light scattering properties of the probe volume have major influence on the return signal strength. The scattering cross section $d\sigma/d\Omega(\phi, \lambda, d_p)$ of a particle is in general dependent on the scattering angle ϕ , the wavelength λ and the particle diameter d_p [2]. For a lidar,

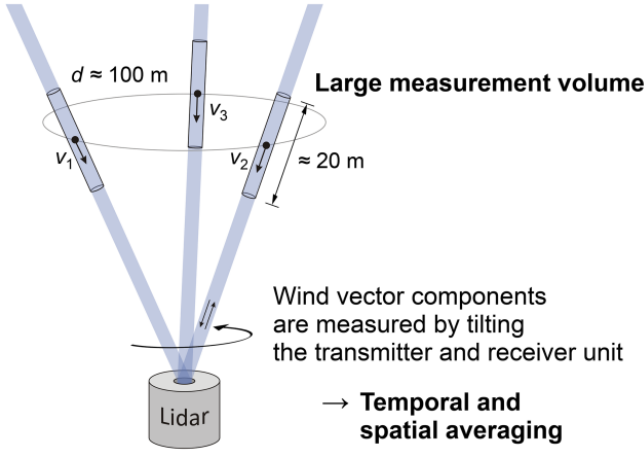


FIG. 2. Typical monostatic scanning lidar setup. Figure from [13].

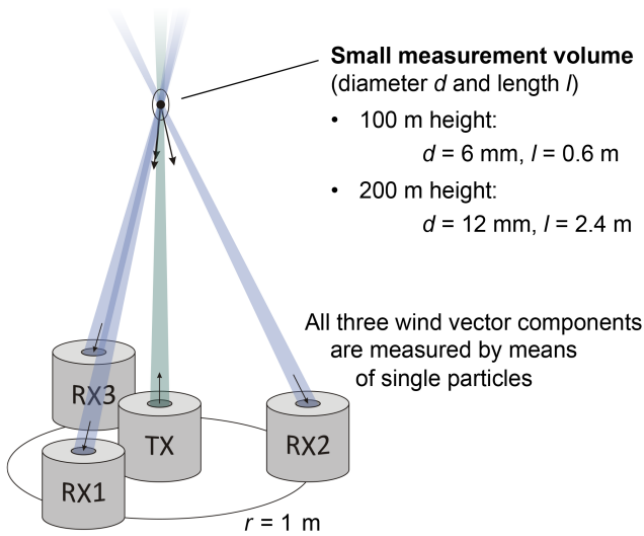


FIG. 3. Bistatic lidar setup. The probe volume length is reduced from 20 m to 0.6 m (by 97%). Figure from [13].

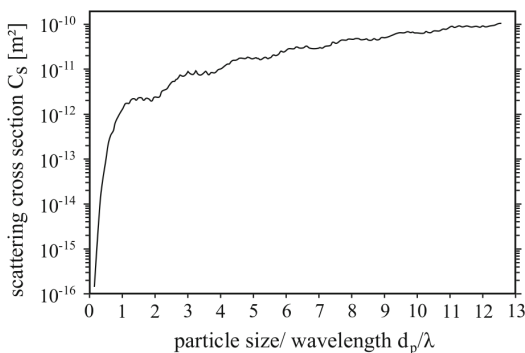


FIG. 4. Scattering cross section versus particle size. Figure by [14].

ϕ is usually equal or close to the backscattering angle $\phi = \pi$. The scattering strength depends on the ratio of particle size to laser wavelength, as shown in Fig. 4, and on the particle refractive index [14]. A typical classification is made for particle diameters smaller λ_0 (Rayleigh domain) and particle diameters larger λ_0 (Mie domain). The Rayleigh domain includes scattering on air molecules (nitrogen, oxygen, ...) and its intensity varies as λ_0^{-4} [1]. This scattering can become relevant for short wavelength lasers, but will be of less to none importance for longer (near infrared) wavelength lidars [1]. Naturally occurring aerosols like droplets, soot, sea-salt, dust and soil particles are mostly covered by the Mie domain, where the scattering intensity varies in a complex relation with particle size and refractive index. Overall, the trend is that the scattering cross section increases with particle diameter and refractive index [15–17]. The total scattering effect of the probe volume on the return signal is described by the backscatter coefficient β , which includes the contribution of all present particle species and is thereby dependent on the particle concentrations [1].

The probe volume describes the region in space, from which reflected light is effectively collected by the receiver. For a monostatic setup, the lidar optics are able to focus on a volume characterized by a half-width at half maximum intensity of

$$\Gamma = \frac{\lambda_0 R^2}{\pi a^2}, \quad (1)$$

where R is the distance from the lidar to the probe volume and a is the laser beam width at output lens or aperture [8, 10]. This shows that the probe length in the order of 2Γ increases with observation distance squared. In Fig. 1, it is shown that the laser intensity forms a Lorentz distribution around the lidar focal point [12].

The return laser power is generally given by

$$P_s = K_s \frac{O(R)}{R^2} \beta(R) T(R), \quad (2)$$

where K_s represents the performance of the lidar system (including laser transmitter power P_T and probe volume size), $O(R)$ is the laser-receiver-field-of-view overlap function, $\beta(R)$ is the aforementioned backscatter coefficient and $T(R)$ is the transmission function, giving the amount of light, which is removed by absorption and undesired scattering on the path between probe volume and lidar [1]. The probe volume size increases with R^2 , which counteracts the R^{-2} , dependence of P_s . An approximation for the received signal power for coherent CW laser is given by $P_s = \pi P_0 \beta(R) \lambda_0$, which is independent of observation range [10].

Lidars can be configured in monostatic setup, where transmitter and receiver share the same optical path and

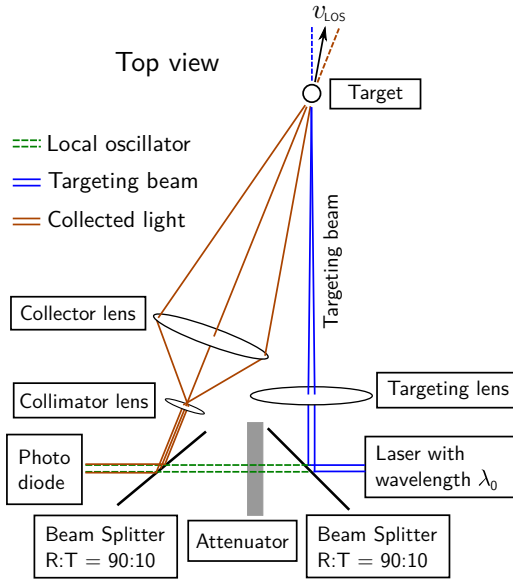


FIG. 5. Schematic of the used bistatic lidar setup. The geometry at the focal point and the orientation of the lidar line-of-sight velocity is further illustrated in Fig. 8.

elements (also called "transceiver") or in bistatic setup, where the transmitter and receiver are separated. Figure 2 by Oertel *et al.* shows a typical monostatic scanning lidar operated from the ground [13]. By beam focusing, the lidar is able to measure at different ranges, approx. from 10 to 200 m. By tilting and rotating the transceiver, a circle of measurement positions can be scanned and the vertical and horizontal velocity components can be determined. The probe volume length depends on the target range and amounts to approx. 20 m for 100 m measurement height. In horizontal direction, the averaging is done over a large circle with diameter of approx. 100 m. Oertel *et al.* show possible advantages of the bistatic setup (cf. Fig. 3), for which the lidar probe volume is reduced by significant amounts and the possibility is provided to measure all three velocity components simultaneously, using a single laser source (TX) and three separated detectors, (RX1, RX2 and RX3) [13]. A smaller probe volume leads to less particles contributing to the back scattered light. While volume averaging effects are minimized, the total reflected light intensity and thus the signal strength is reduced, which increases the difficulty of acquisition and data processing.

B. Lidar setup

This section presents the bistatic lidar setup used in this study, as shown in Figs. 5 and 6. The laser light is split at the first beam splitter into the reference beam

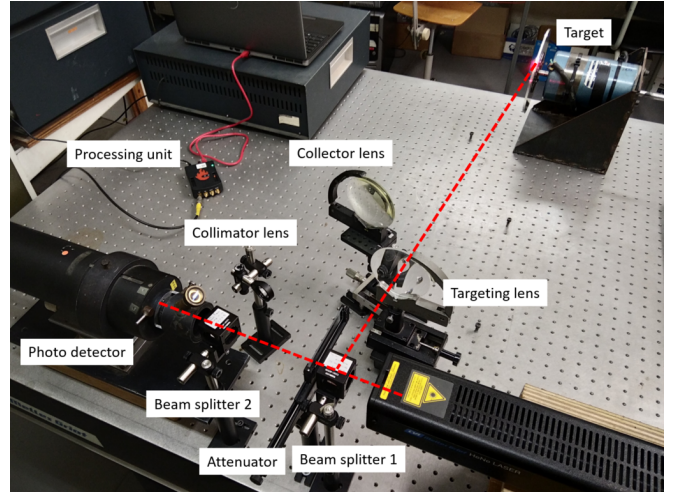


FIG. 6. Illustration of the used bistatic lidar setup.

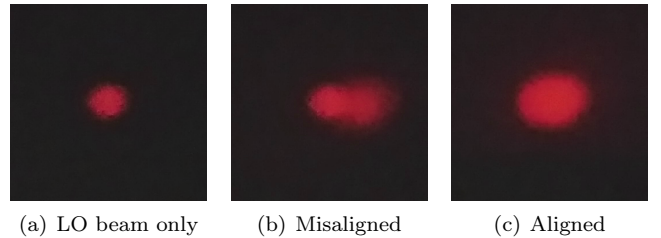


FIG. 7. Images of local oscillator and collected light on a black screen.

(local oscillator) and the target beam. The LO directly passes the adjustable attenuator with optical depth exponent between 0 and -4 and the second beam splitter and is then collected by the photo detector, which includes a pin hole with adjustable size in front of the photosensitive material. Both beam splitters have reflection to transmission ratios of R:T = 90:10. The target beam is focused by a lens with focal length 72.5 cm onto the target, where the light is scattered in all directions. Part of the backscattered light is collected by the collector lens with diameter 10 cm and focal length 16.5 cm. After passing the collector lens, the converging collected light is collimated by a small lens with focal length 1.5 cm to generate a concentrated beam of parallel light, which is redirected by the second beam splitter and brought to interference with the local oscillator at the photo detector. The careful collimation of the collected light and the alignment with the reference beam is of crucial importance for the working principle of the lidar. Target and local oscillator beam have to be parallel and overlapping not only at the photo detector, but over a the whole path starting at the second beam splitter. This can be checked by removing the detector and investigating the beam path over a longer range. Figure 7 shows the im-

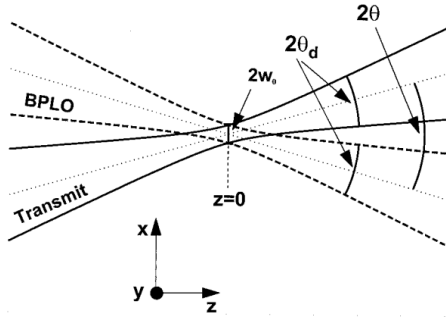


FIG. 8. Crossing of the transmitted target beam and the direction focused by the collector lens. This direction is characterized by the so called virtual back-propagated LO beam (BPL0). Figure from [20].

age of the local oscillator and the collected light beam for aligned and misaligned cases on a black screen. The light intensity is converted to a voltage signal at the photo detector and passed to the processing unit, which includes an analog-to-digital (ADC) converter. Data processing is further described in Sec. II C. The presented setup is motivated by [9], but was extended by the targeting lens, which focuses the beam on the target, increases the laser power in the focal point, and decreases the probe volume length. This adjustment proved to enhance the signal strength.

The used laser is a visible HeNe laser with a vacuum wavelength of $\lambda_{\text{vac}} = 632.991 \text{ nm}$ (red light) [18]. The laser power was determined during the measurements with an optical power meter to be $P_T = 34 \text{ mW}$. The refractive index of air under standard conditions ($p = 1 \text{ atm}$, $T = 15^\circ \text{C}$) is $n_0 = 1.000277$ [19]. The refractive index varies with air density and thus with pressure and temperature. Using formulas of Ciddor [19], the total maximum variation of the refractive index in the ranges of $T \in [10, 30]^\circ \text{C}$ and $p \in [99\,000, 103\,000] \text{ Pa}$ were calculated to be 0.003%. This corresponds to a maximum deviation in Doppler frequency of 2000 Hz for a target velocity of 20 m/s. Considering the typical spectral bin resolution of 30 000 Hz, the variation in refractive index due to temperature and pressure can be neglected in the present case. The value of n_0 is thus used to determine the laser output wavelength of $\lambda_0 = \lambda_{\text{vac}}/n_0 = 632.816 \text{ nm}$. The conversion from velocity to Doppler-frequency is therefore given by $f_D = v_{\text{LOS}} \times 3.16 \text{ MHz}/(\text{m s}^{-1})$.

Figure 8 by Harris *et al.* illustrates the probe volume of the bistatic setup in detail. To be detected by the lidar, the target needs to be in the region, where the transmission beam crosses with the field focused by the collector lens. The collector focusing effect can be represented

by the so called virtual back-propagated local oscillator (BPL0), leading to the optically equivalent crossing of two beams with a certain width distribution to define the probe volume. In the presented setup, the angle between the beams is given by $2\theta = (8 \pm 2)^\circ$. The lidar with a single beam and single collector measures only the line-of-sight velocity, the direction of which is defined by the bisection between the target beam and the BPL0, i.e., deviates from the target beam by $\theta = (4 \pm 1)^\circ$.

The photo detector and the laser introduce several noise sources, including dark noise, photon shot noise and laser relative intensity (RIN) noise, which will lead to characteristic distortions in the frequency spectrum. A good signal to noise ratio decreases the necessary number of sampling intervals. The photon shot noise increases with intensity of the local oscillator. Consequently, one cannot increase the LO intensity arbitrarily to boost the signal strength, but a certain ratio of P_{LO} and P_s must be fulfilled to acquire a reasonable signal to noise ratio. In practice, a ratio P_s/P_{LO} in the range of 1/2 to 1/4 proved to produce the best signal-to-noise ratio for the given setup. It shall be noted that for conventional lidars, the LO-power is usually much higher than the power of the collected light [2].

C. Data processing

The voltage signal of the photo detector is processed by a Red Pitaya STEMlab 125-14 measurement board, including an ADC converter with sampling frequency $f_s = 125 \text{ MHz}$ [21]. The corresponding Nyquist frequency of 62.5 Mhz allows to determine target LOS-velocities of up to 20 m/s for the HeNe laser wavelength of 632.8 nm. The board is controlled remotely via network TCP connection. Koheron provides code examples for a python API [22], which were adjusted and extended during the project. Signal processing after the ADC is performed directly on the Red Pitaya board using an Field-Programmable Gate Array (FPGA) interface. Pre-compiled instruments for the FPGA are provided by Koheron, as well, and were used for data acquisition and on-board Fourier analysis and spectral block averaging. The FPGA modules were incorporated in the self-developed python scripts and controlled via the network interface.

The general data processing algorithm, how to convert the digital photo detector voltage time series into a time series of measured velocities, is presented in Fig. 9. The voltage time series is split into several blocks of N_{bins} data points. For each block, the discrete frequency spectrum is generated via Fast-Fourier-Transformation (FFT) and then averaged bin-wise to yield the mean

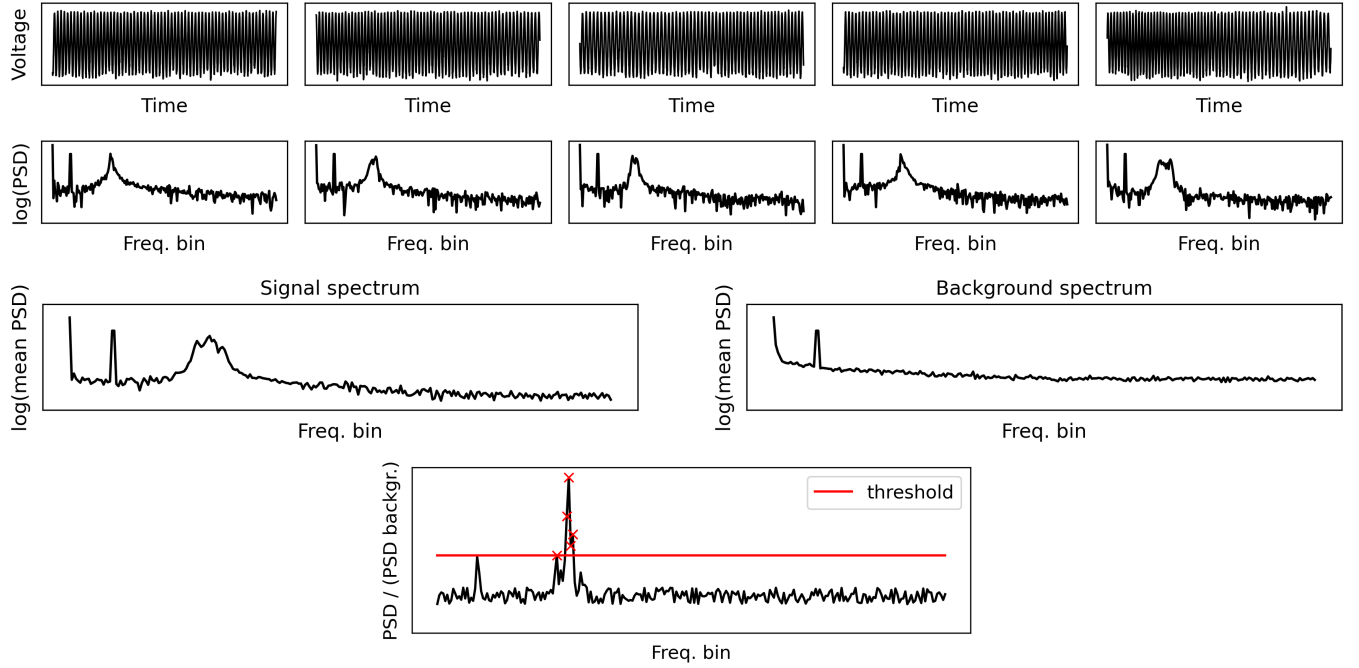


FIG. 9. Data processing procedure. The photo detector voltage time series is split into several blocks. DFT spectra are generated for each block and then averaged bin-wise to yield the mean PSD spectrum. Noise whitening is achieved by dividing the average signal spectrum by a previously recorded background spectrum. A constant threshold is applied to the normalized spectrum to remove noise.

PSD spectrum. Similarly, a background spectrum (without Doppler peaks) is generated. The background might contain characteristic noise sources of the reference laser (RIN noise), the photo detector and the electronics. Noise whitening is achieved by dividing the average signal spectrum by the background spectrum, leading to the normalized spectrum. A constant threshold is applied to the normalized spectrum to remove noise contributions. The threshold is defined as $\mu_{\text{bg}} + N_\sigma \sigma_{\text{bg}}$, where μ_{bg} and σ_{bg} are the background PSD mean and average standard deviation, respectively, and N_σ is the threshold factor. All frequencies above the threshold are considered valid Doppler frequencies, because all particles residing in the probe volume contribute to the Doppler spectrum. Under atmospheric conditions, the Doppler peak is broadened, because scattering particles in the probe volume move with different relative velocities due to local turbulence. The task is now to apply a frequency estimator to determine a single effective frequency for the given averaged spectrum and convert it to a single velocity. Several methods are available for peak finding and analysis (cf. [24]). In this work, the basic and fast mean, median and max estimators are applied, as described in [23]. In the course, one velocity value is determined for each averaged spectrum by applying the Doppler formula. The streaming rate of the resulting velocity time series de-

pends on the number of bins and the number of averaged spectra. For conventional lidars, a typical value for the streaming rate is 50 Hz, which enables statistical treatment and assessment of turbulence properties. In this study, a streaming rate of 30 Hz was achieved for velocity live-stream application and 60 Hz for the analysis of spectra recorded without live-streaming.

D. Validation with flywheel target

A metallic, motor driven flywheel with diameter 19.8 cm and width 0.5 cm, shown in Fig. 10, is used for lidar validation. The wheel motor rotation speed can be controlled by the supplied voltage. Knowing the rotation rate and the wheel perimeter, the tangential velocity of the wheel surface can be calculated and projected onto the lidar line-of-sight velocity. The lidar setup for measuring the flywheel velocity, including a sketch of the wheel side view is presented in Fig. 11. The lidar is focused on the wheel edge, which, due to its roughness, scatters the light backwards in all directions, acting like many small particles concentrated on the surface. The scattered light is collected and analyzed as usual. The flywheel acts as a target with defined velocity, which remains in the focal point. The total angle between the

wheel horizontal velocity and the lidar line-of-sight velocity is composed of the angle between the target lens and the normal, $\alpha_1 = (7 \pm 1)^\circ$, and the half-angle between target and collector beam $\theta = (4 \pm 1)^\circ$. The total projection angle is thus $\alpha_{\text{wheel}} = (11 \pm 2)^\circ$.

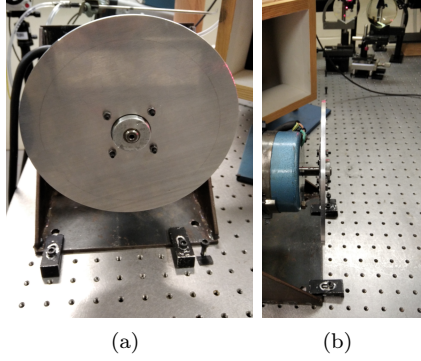


FIG. 10. Flywheel with diameter 19.8 cm and width 0.5 cm.

E. Particle tracking velocimetry of water droplets in an open wind tunnel stream

Additionally to the flywheel validation, measurements with water droplets are conducted to assess the capabilities of the lidar. Falling droplets of 2 mm diameter are created at a defined frequency of 10 Hz, using a piezo-electric droplet generator. During their fall, the droplets cross the stream of an open wind tunnel, leading to an horizontal acceleration and corresponding curved trajec-

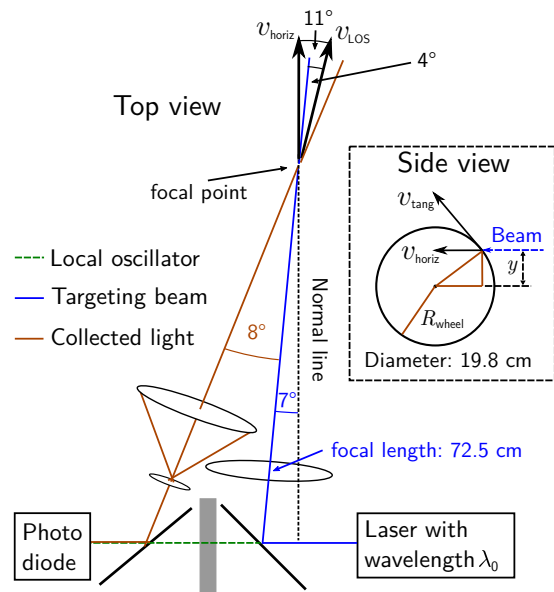


FIG. 11. Bistatic lidar setup focused on the flywheel. The lidar components are labeled in Fig. 5.

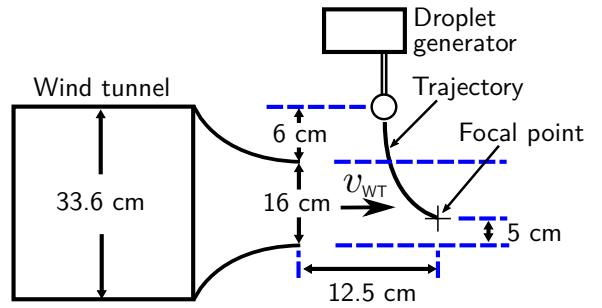


FIG. 12. Side view of the falling droplet setup with the droplet generator mounted above the open wind tunnel outlet.

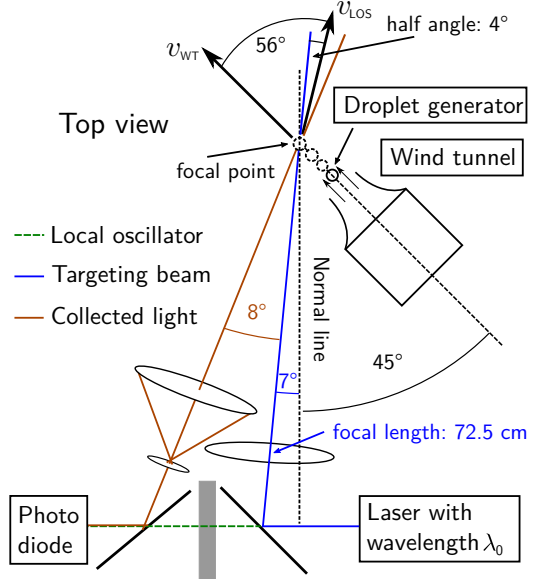


FIG. 13. Droplet generator in front of the open wind tunnel. The lidar components are labeled in Fig. 5.

tory, as illustrated in Fig. 12. The droplet source is kept at a constant height above the wind tunnel entrance. The horizontal position is however adjusted, according to the set wind tunnel speed, such that the droplets cross the lidar focal point, which remains at a constant distance to the wind tunnel outlet.

The setup geometry is defined in Figs. 12 and 13. Making the assumption that the wind tunnel flow is following the direction of the wind tunnel outlet in the core region and that the droplet horizontal acceleration is perfectly aligned with the wind tunnel core flow, it is possible to determine the horizontal velocity direction with respect to the lidar normal line by measuring the alignment of the wind tunnel with respect to the optical table. Evidently, these assumptions introduce significant sources of uncertainty, which are considered, when presenting the results. The total angle between the wind

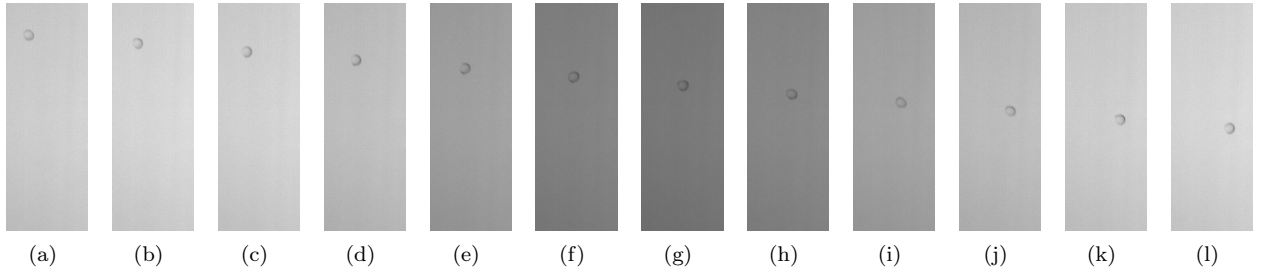


FIG. 14. Cutouts of twelve consecutive images, showing a falling droplet generated with the droplet generator passing the wind tunnel stream. The camera recording rate is 1000 fps. The droplet diameter is approx. 2 mm. The darkening and brightening of the white background is due to the background light flickering with the electrical power line frequency of 50 Hz.

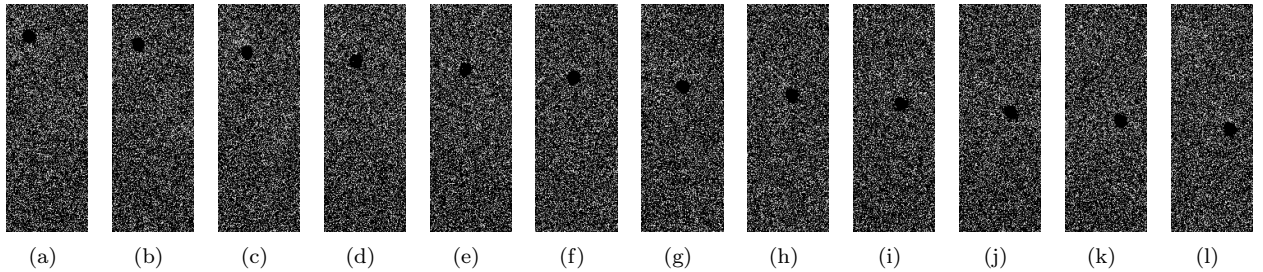


FIG. 15. Cutouts of the same twelve consecutive images of Fig. 14, showing a falling droplet passing the wind tunnel stream after removing the first two POD modes. The darkening and brightening of the white background due to the background light flickering has been removed by the POD. The droplet is visible and trackable as a continuous black shape.

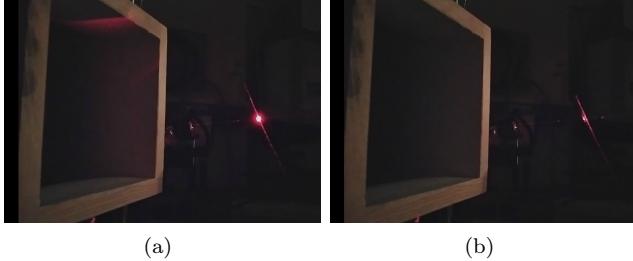


FIG. 16. Falling droplets in wind tunnel stream. In (a), the droplet exactly hits the lidar focal point, while in (b), the droplet misses the focal point.

tunnel velocity (and thus approximately also the droplet horizontal velocity) and the lidar line-of-sight velocity is composed of the angle between the target lens and the normal, $\alpha_1 = (7 \pm 1)^\circ$, the half-angle between target and collector beam $\theta = (4 \pm 1)^\circ$ and the angle between wind tunnel and the normal, $\alpha_2 = (45 \pm 3)^\circ$. The total projection angle is thus $\alpha_{WT} = (56 \pm 4)^\circ$. The wind tunnel velocity can be adjusted by setting the motor speed and the free stream velocity is measured for each setting with a Prandtl tube at the focal point. For the used wind tunnel, the free stream velocity at focal point is limited between 4.0 m/s and 7.2 m/s.

Example images of droplets close to the focal point are shown in Fig. 16. It shall be emphasized that the wind tunnel stream is highly unstable, leading to fluttering and large deviations between individual droplet trajectories, even though all droplets are generated with the same size. Since the focal point of the bistatic lidar is quite small, careful adjustment of the horizontal position of the droplet source is of major importance to increase the number of droplets actually hitting the focal point. Even for an optimal adjustment of the droplet generator position, the hit rate is however still very low.

To validate the lidar measured particle velocity, the droplets are recorded by a high speed camera at 1000 fps and the trajectories are analyzed by particle tracking velocimetry (PTV). For that purpose, a backlighting technique is used and the camera is adjusted such that the droplets are in focus all along their trajectories. This ensures that the camera is positioned perpendicular to the droplet paths, indicated in Fig. 12, within an uncertainty corresponding to the camera's depth of field.

As an example of a recorded droplet trajectory, twelve consecutive images are shown in Fig. 14. The generation frequency of 10 Hz is set such that only one single droplet is present in the camera field of view at any time. The droplet moves less than one diameter (of approx. 2 mm)

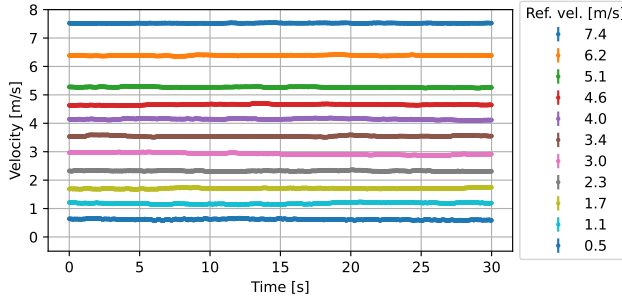


FIG. 17. Lidar measured velocity time series for the flywheel target after removing invalid data points. The line-of-sight velocity of the wheel surface is given in the legend.

per image. The periodic darkening of the white background is caused by the background light flickering with the electrical power line frequency. The camera image series are treated by proper orthogonal decomposition (POD). Removing the first two POD modes eliminates the light flickering and leaves the droplets as continuous black shapes on a noisy background, as can be seen in Fig. 15. The processed images can then be analyzed by particle tracking velocimetry. A basic particle tracking algorithm was developed to compute droplet trajectories and velocities, by identifying the local region with the most black pixels in each frame of the POD processed images and determining the corresponding region centers as the droplet positions. Knowing the center positions and the time step between consecutive images, it is possible to determine the horizontal and vertical velocity components from the recorded images, using a second order central difference scheme.

III. RESULTS

This section presents validation of the lidar against a flywheel with defined rotation speed (Sec. III A) and conducted lidar velocity measurements of droplets driven by an open wind tunnel compared to particle tracking velocimetry (Sec. III B).

A. Lidar validation with flywheel target

Lidar measurements of 30 seconds were conducted for 11 different flywheel motor voltage values ranging from 0 to 7 V, corresponding to LOS velocity values from (0.5 ± 0.2) m/s to (7.4 ± 0.4) m/s. For each measurement, a series of averaged DFT spectra with 4096 frequency bins (at a sampling rate of 125 MHz) was acquired with the measurement board. Averaged spectra

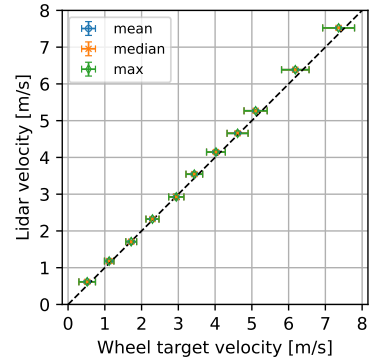


FIG. 18. Validation of the velocity measured with the lidar against the flywheel line-of-sight velocity. The lidar values are averaged over 30 seconds after removal of invalid data points and outliers. The three different frequency estimator methods are indicated in the legend, but do not show detectable deviation.

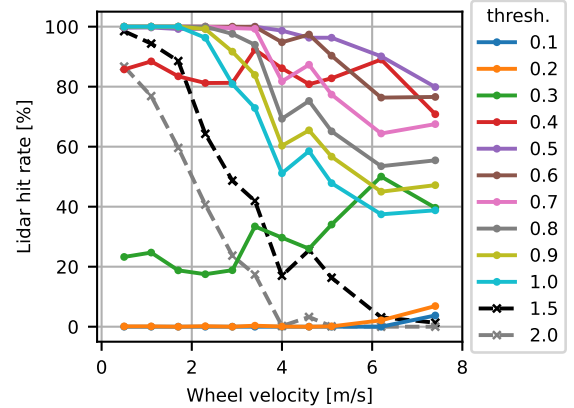


FIG. 19. Lidar hit rate (ratio of valid points after outlier removal and total data points) for flywheel velocity measurements. The threshold factor N_σ is indicated in the legend.

are generated by bin-wise averaging over 512 consecutive DFT spectra. Each averaged spectrum comprises one velocity data point after noise whitening and peak finding analysis. The velocity streaming rate is thus 59.6 Hz. The 11 time series of 30 seconds, each containing approx. 1800 velocity data points, are shown in Fig. 17, after removing zero-velocity values, including points, where no frequency peak of the normalized spectrum reached the threshold. The time series are well separated and show only minor fluctuations around their respective mean. The time-averaged lidar velocities agree well with the reference values for all three applied frequency estimator methods, as illustrated in Fig. 18. Since the spread of the lidar velocities around the mean is relatively small and the bin resolution is only 0.01 m/s for 4096 bins, the

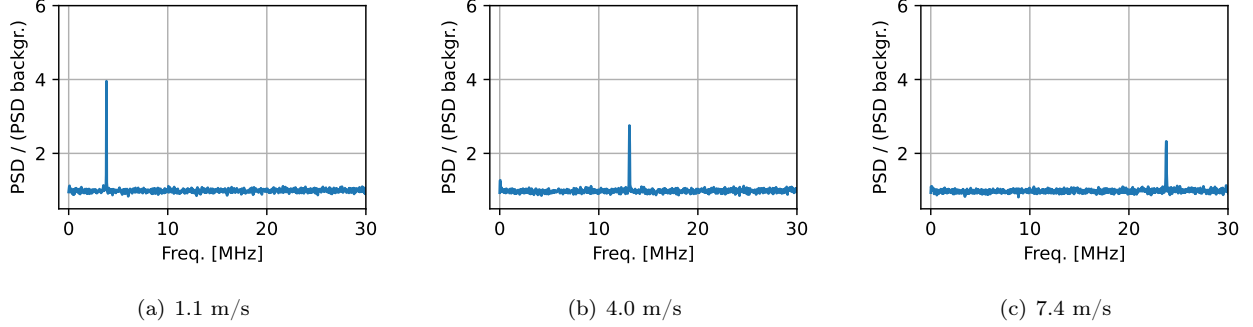


FIG. 20. Example Doppler spectra of the flywheel target. The wheel LOS velocity is given in the figure sub captions. For the shown spectra, the wheel velocity is matched by the measured lidar velocity.

optical lidar technique shows very small uncertainties, compared to the target wheel uncertainties, which stem from the wheel calibration and the uncertainty of the projection angle. Considering the 95% confidence intervals, the lidar measurements are successfully validated by the flywheel.

The ratio of valid data points after additional outlier removal and total data points will be denoted as lidar hit rate. The hit rate can be influenced by the threshold factor, as shown in Fig. 19. A lower threshold factor leads to more detected peaks. On the other hand, for small thresholds, more noise values will enter the evaluated range above the threshold. A threshold factor of 0.5 was chosen for the wheel calibration, leading to a balance between noise removal and hit rate. The hit rate is generally declining with higher wheel speeds, because noise increases and the Doppler peaks become less pronounced, as can be seen for example burst spectra in Fig. 20. The reasons for declining peak height with speed are mostly connected to imperfections of the wheel: The disc is not perfectly round, leading to deviations in the diameter and thus tangential velocity and the edge is additionally wobbling parallel to the rotation axis. For higher speeds, a larger area of the wheel is covered by the laser beam during acquisition of each velocity point. Thereby, the number of roughness elements contributing to the peak is increased and the peak is broadened, because the different roughness elements have slightly different velocities due to diameter variations and wobbling. This leads to a reduction of the peak maximum value.

By moving the flywheel back and forth in direction of the target beam from a point with strong Doppler signal until the signal was not detectable anymore, a probe volume length of approx. 2 mm can be coarsely estimated for the bistatic setup. The theoretical probe volume length of 5.3 cm calculated by Eq. (1) for a monostatic setup with target distance of 72.5 cm is thus reduced to

$0.2/5.3 = 4\%$ for the bistatic setup. This can be compared to the estimated reduction to 3% from Oertel et al. [13] (cf. Figs. 2 and 3), which falls in the same order of magnitude. The reduction in probe volume length will additionally depend on setup parameters, e.g. the angle between target and collector beam (8° vs. 0.6°), target distance (0.725 m vs. 100 m) and beam diameter (2 mm vs. 35 mm), comparing this work and the work of [13].

B. Lidar validation by particle tracking velocimetry of water droplets driven by an open wind tunnel

Lidar measurements were taken for 3 different wind tunnel velocities of 4.0 m/s, 6.0 m/s and 7.2 m/s with a fixed droplet generator frequency of 10 Hz, leading to droplet sizes of approx. 2 mm. For the same wind tunnel and droplet generator settings, the trajectories were recorded for 4 seconds at 1000 fps and analyzed by particle tracking velocimetry. Due to the unsteadiness of the flow in front of the open wind tunnel and instabilities in the wind tunnel motor performance, the trajectories of the particles are not uniform and strong fluttering can be observed, as shown in Fig. 21.

Horizontal and vertical velocity components are computed from the particle trajectories and time intervals between consecutive frames, using a central finite difference scheme. Velocity arrows of three arbitrarily selected trajectories per wind tunnel setting are shown in Fig. 22 to elucidate the procedure. To compare the results with lidar measurements, it is necessary to obtain the horizontal velocities at the focal point. This is done by selecting the droplet frame from each trajectory, for which the y -position is closest to the laser beam height. The velocity component at this position is averaged over the selected frames, amounting to a maximum of 38 frames for 4.0 and 6.0 m/s, and 37 frames for 7.2 m/s. A convergence study shown in Fig. 23 shows that convergence

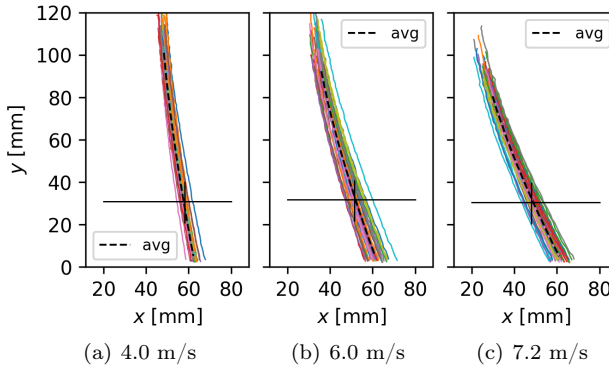


FIG. 21. Trajectories of droplets falling in front of an open wind tunnel evaluated by particle tracking velocimetry. The lidar beam height and focal point are indicated by the two crossing black lines in each graph. The wind tunnel free stream velocity at the focal point is given in the sub captions.

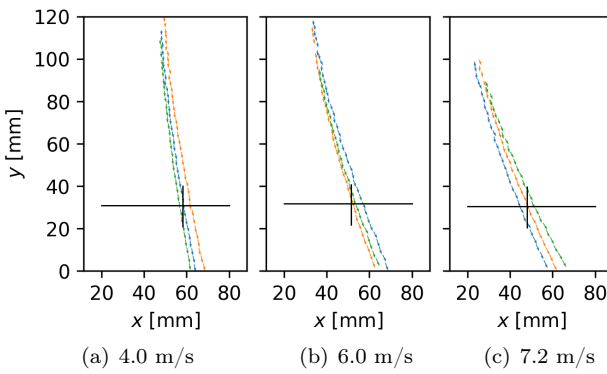


FIG. 22. Three arbitrarily selected droplet trajectories per wind tunnel setting from Fig. 21, indicating the determined velocity vectors at each time step. The lidar beam height and focal point are indicated by the two crossing black lines in each graph. The wind tunnel free stream velocity at the focal point is given in the sub captions.

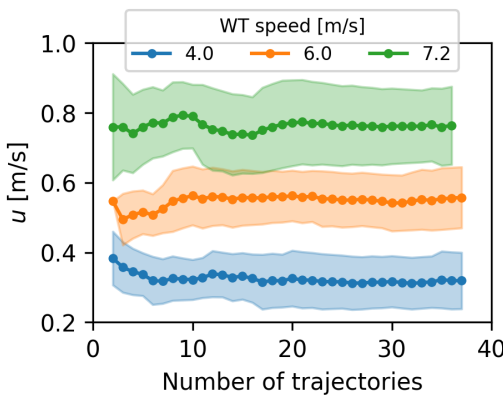


FIG. 23. Convergence of the average horizontal velocity component at focal point height, determined from the PTV trajectories. The standard deviation is indicated by the shaded areas.

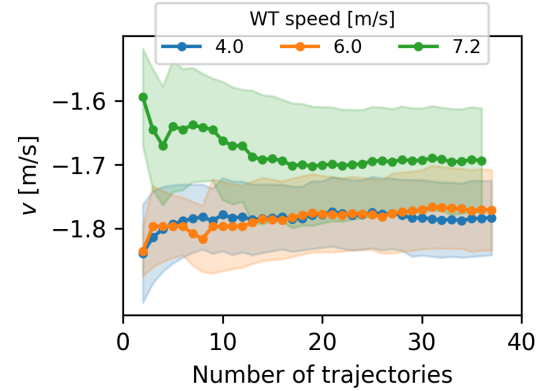


FIG. 24. Convergence of the average vertical velocity component at focal point height, determined from the PTV trajectories. The standard deviation is indicated by the shaded areas.

is reached after approx. 30 trajectories. Averaging over all available trajectories leads to horizontal speeds at the focal point height of (0.3 ± 0.1) m/s, (0.6 ± 0.1) m/s and (0.8 ± 0.2) m/s. After projecting onto the lidar LOS direction with the projection angle indicated in Fig. 13, velocity components of (0.2 ± 0.1) m/s, (0.3 ± 0.1) m/s and (0.4 ± 0.1) m/s remain for the three wind tunnel settings, which can be compared to the lidar measurements.

Analogously, the vertical velocity convergence is analyzed at focal point height, as shown in Fig. 24. While the vertical component shows similar behavior for the two lower wind tunnel speeds, its magnitude is reduced for $U_{WT} = 7.2$ m/s. The offered interpretation is that the droplets are affected by a faster wind tunnel stream, following the horizontal flow more closely and thereby deviating from the vertical free fall curve. However, it can be seen that the droplets are far too large to directly follow the ambient flow. For the given wind tunnel speeds of 4.0, 6.0 and 7.2 m/s, the droplets reach maximum horizontal velocities of 0.4, 0.6 and 0.9 m/s, respectively before leaving the wind tunnel zone. With a vertical reference velocity of 1.7 m/s, the Stokes number can be estimated as

$$St = \frac{\tau}{t_{ch}} = \frac{\rho_p D_p^2}{18\mu_f} \frac{1}{t_{ch}} \approx 130, \quad (3)$$

where ρ_p is the particle (water) density, $D_p = 2$ mm the particle diameter and μ_f the dynamic air viscosity. The characteristic time scale t_{ch} is estimated by the time a falling droplet requires to pass the wind tunnel opening from top to bottom, i.e., $t_{ch} = H_{WT}/\langle v \rangle = (16 \text{ cm})/(1.7 \text{ m/s}) = 0.09 \text{ s}$. The large Stokes number of 130 and large viscous lag time $\tau = 12 \text{ s}$, support the observation that the particles do not follow the ambient flow.

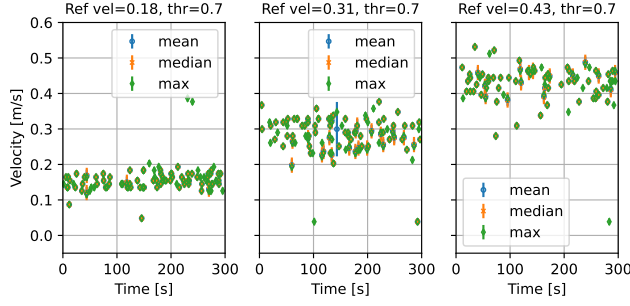


FIG. 25. Lidar measured velocity time series for the falling droplets, after removing invalid values. Each data point corresponds to the Doppler burst of one particular droplet hitting the lidar focal point. The droplet LOS velocity (in m/s) evaluated by PTV and the chosen threshold factor are given in the plot titles.

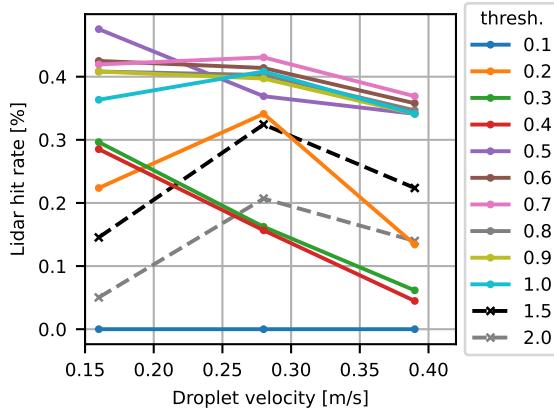


FIG. 26. Lidar hit rate (ratio of valid points after outlier removal and total data points) for velocity measurements of droplets in the open wind tunnel stream. The threshold factor is indicated in the legend.

Lidar measurements of 300 seconds were conducted for each of the three wind tunnel settings, with the same acquisition parameters described in Sec. III A. Each velocity time series contains approx. 18 000 data points. After removing zero-velocity values, spectra, where no frequency peak reached the applied threshold, and values with a relative standard deviation larger than 30%, the number of velocity points is drastically reduced. The applied limit for relative standard deviation is not following a systematic procedure, but is chosen by visual analysis of its effect on the resulting time series for low thresholds, were the number of detected noise peaks and therefore the standard deviation of the frequency estimator methods is highest. This limit needs to be reevaluated when analyzing lidar measurements conducted under varying conditions and with differing targets. The resulting time

series are shown in Fig. 25. Here, each data point corresponds to the detected Doppler burst of one particular droplet hitting the lidar focal point. Only a few individual points remain after the filtering procedure, which can clearly be identified as outliers. For a total measurement time of 300 s, an average number of about 80 usable values remain out of 18 000 possible spectra, leading to a hit rate of approx. 0.4% (cf. Fig. 26). After evaluating the effect of the threshold on the hit rate (as for the flywheel in Sec. III A), a threshold value of 0.7 was chosen for the droplet measurements.

The reason for the low lidar hit rate is the small probe volume of the bistatic setup, i.e., that the droplets have to hit the focal point exactly to be detected. Since the trajectories in the wind tunnel stream flatter strongly, most of the droplets miss the focal point in either, vertical or horizontal direction. Additionally, the background, laser and photo detector noise sources close to the low frequencies ($f_D < 2$ MHz) render a significant amount of data points unusable. It shall be emphasized that choosing the right background spectrum is of major importance to obtain any meaningful velocity values. In the present case, the background noise level is dominant in certain low frequency domains, including [0.03, 0.4] MHz and [1.05, 1.25] MHz. The observation is made that whenever a droplet hits the focal point and the target light mixes with the reference beam at the photo detector, not only a Doppler peak can possibly be detected, but the background noise characteristic is enhanced as well, especially in the indicated intervals. Additional peaks in the same order of magnitude as the true Doppler bursts will be induced by noise enhancement in the recorded spectra, inducing artificial detected signals as well as a major spread of the frequencies above the threshold. This behavior implies that for the investigated setup a background spectrum, which is recorded from the local oscillator alone is not sufficient for successful background removal.

To obtain meaningful results, a method described in [23] is used, where the background spectrum is evaluated from the lidar spectra recorded during the actual velocity measurements by analyzing the statistics in each frequency bin and setting the median value for each bin as the background. This can only be done for spectra series with sparsely occurring peaks (i.e. low hit rate). The median filters the actual Doppler bursts as outliers and returns a meaningful background PSD for each bin. Furthermore, as a crucial step, characteristic noise intervals in the range of [0.03, 0.4] MHz and [1.05, 1.25] MHz were detected by hand and specifically pronounced in the background PSD spectra by adding an additional value of 0.44 bin-specific standard deviations to the respective bins. This enhancement factor was varied and the effect

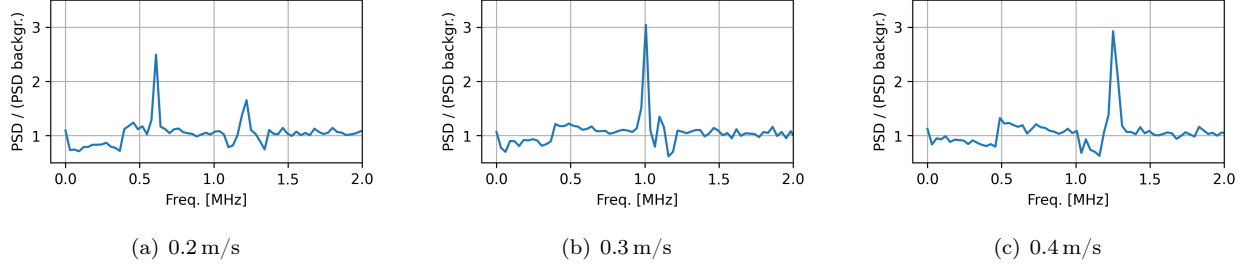


FIG. 27. Example Doppler spectra for falling water droplets in the open wind tunnel stream. The figure sub captions indicate the droplet LOS velocity evaluated by PTV, which is matched by the lidar measured values. Besides the Doppler peak, a laser RIN noise peak can be seen in the range from 1.1 to 1.2 MHz.

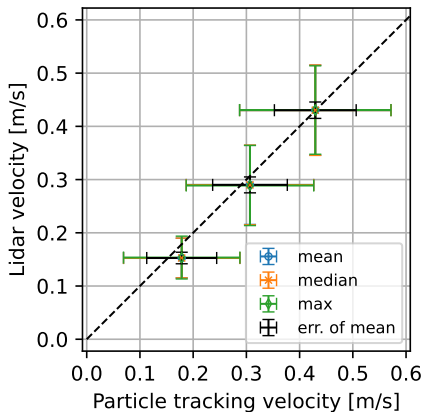


FIG. 28. Validation of the droplet velocities measured with the lidar against particle tracking velocimetry. The three different frequency estimator methods are indicated in the legend. The colored (larger) errorbars indicate 95% confidence intervals, including the full standard deviation of data points, while the black errorbars include the reduced standard deviation of the mean.

on the resulting Doppler burst spectra was investigated (cf. Fig. 27). The value of 0.44 was chosen, because it prohibits the characteristic, noise-induced peaks from reaching the threshold in case of the optimal threshold factor. The effect of this method can be seen in Fig. 27, where the normalized spectra show values smaller than one for parts of the identified intervals, being divided by a artificially enhanced background. Additionally, the true Doppler burst peaks are visible, as well as the emerging RIN-noise peak in the range [1.05, 1.25] MHz. Without modifying the background spectrum to dampen the intensity induced noise enhancement, the emerging peaks would cross the threshold and render the selected spectra effectively unusable. Exclusion of certain noise-laden bin regions from the Doppler peak finding algorithm is also applied in [23].

After additional outlier removal, the lidar time series from Fig. 25 are statistically analyzed. The resulting mean values are compared with the reference PTV measurements in Fig. 28. Although the spread of both, lidar and PTV values is significant, the lidar is able to detect an increase in droplet velocity and the mean values coincide within the estimated uncertainties, when considering the 95% standard error of the mean, shown as black bars in Fig. 28.

IV. CONCLUSIONS AND OUTLOOK

The purpose of the presented work was the development and construction of a miniature lidar system starting from a number of basic optical components, the validation of the lidar working principle and the assessment of the lidar capabilities, as well as the implementation of the necessary data processing software. After selecting and testing several configurations, a bistatic setup was chosen and validated by a flywheel target with adjustable velocity and by particle tracking velocimetry of falling water droplets in an open wind tunnel stream.

The lidar was successfully validated with the flywheel in a velocity range from 0.5 to 7.4 m/s. The noise removal threshold factor proved to have major influence on the hit rate (ratio of valid lidar points and total data points). An optimal threshold value of $N_\sigma = 0.5$ was determined for the wheel measurements. The hit rate is declining with target velocity and reaches 80% at the maximum tested velocity. The flywheel proved to be a functional validation instrument. The precision can however be improved by using a stabilized voltage source for the wheel motor with lower reading uncertainty and by using a wheel setup with improved motor, shaft and bearings to assure a steady rotation and less fluttering in the cross direction.

The lidar measurements of falling droplets in an open

wind tunnel stream proved to be more delicate due to strong fluttering and fluctuations of the trajectories in the unsteady wind tunnel stream. Since most of the particles miss the focal point, the hit rate is reduced to 0.4% for the optimal threshold factor setting of $N_\sigma = 0.7$. The unsteadiness leads to a large spread in the velocity data, both for the lidar measurements and the reference high speed imaging PTV analysis. Nevertheless, the increase in droplet horizontal velocity with wind tunnel speed can be successfully reconstructed by the lidar. Moreover, the point clouds, as well as the averaged velocities coincide well within the confidence intervals. With 2 mm size, the droplets were too large to follow the wind tunnel stream closely.

The choice of the background spectrum is of major importance to eliminate noise, while keeping the valuable Doppler peak information. Without careful analysis of the laser and photo detector noise characteristics, a meaningful evaluation of the lidar signals was not possible. The recorded background of the local oscillator proved not to be sufficient for valid noise removal. A similar behavior was also reported in [23]. Intensity induced noise enhancement during Doppler bursts and the resulting falsely introduced peaks could be mitigated only by sophisticated modification of the background signal in the characteristic noise regions.

The original incentive of the project was to develop a lidar for wind tunnel measurements. Therefore, it would be necessary to measure the velocity of particles, which are small enough to follow the wind tunnel flow. For the given setup, velocity measurement of a spray of water droplets produced by a vaporizer could not be achieved due to low signal strength of the collected light. This can be attributed to the low laser power of 34 mW and the limited capabilities of the photo multiplier.

A. Outlook and recommendations

Regarding the general setup, the quality of the lidar and the range of applicability can be drastically improved by using a more powerful laser source and an enhanced photo detector. The observation that a power of 34 mW was not sufficient to measure the velocity of small water droplets is supported by reports of Vasiljevic *et al.* [4], who used two 300 mW infrared lasers for drone based applications and Barnhart *et al.* [9], who used a 200 mW visible laser for wind tunnel applications, but was still not able to detect aerosols in unseeded flow. Based on their experiences, it is recommended to use a laser strength of at least 300 mW. Furthermore, the output power and thus the signal strength can be enhanced by

using beam splitters with a ratio of 99:1 instead of 90:10. By directing the light with optical fibers, the flexibility and robustness of the setup can be improved. For drone based applications, a compact, robust and flexible design, based on optical fibers is essential.

The alignment of local oscillator and collected light beam proved to be the most difficult and crucial part. For this delicate setup, high precision optical components are required, which can adjust the horizontal and vertical positions as well as the alignment angle around the horizontal and vertical axes for all lenses and beam splitters in a controlled and precise manner. Providing (ideally electrically controlled) high precision instruments would improve the alignment procedure and boost the signal strength significantly. Overall, the detected Doppler frequencies depend on emerging interference patterns at the photo detector. For a better beam alignment, the individual fringes of the pattern have larger dimensions and the probability is higher that a single fringe is covering the photo detector pinhole, which will lead to a well defined signal. Especially the right distance and relative positioning between collector lens and collimator lens and the mixing of reference beam and signal beam at the second beam splitter is of major importance. Using optical fibers can lead to the same positive effect, because the mixing of LO and collected light can be facilitated by using an optical coupler.

Regarding the falling droplets, a closer correlation analysis, connecting specific droplet trajectories to particular Doppler bursts was not possible, since the PTV and lidar measurements had to be conducted separately from each other. The backlighting components required for the high speed camera imaging would block the lidar path and introduce major disturbances. Investing more time in the setup and background removal, it could be possible to measure simultaneously with lidar and PTV. In this case, single trajectories could be matched with Doppler bursts by the timestamp to evaluate how precise and accurate the velocity of specific droplets can be measured. Thereby, the lidar could be validated much more precisely for particle applications. For sure, the setup can be improved by using a more stable and uniform wind source.

Concerning data processing, additional peak finding algorithms can be tested, both for static analysis of recorded spectra series and for live-velocity-streaming. Additionally, it can be analyzed, which effect the application of different windowing functions on the data time series before the FFT has on the characteristic noise level of the spectra and the final velocity results. In the current state, averaging of FFT-generated DFT spectra is

conducted on the Red Pitaya measurement board and the series of averaged spectra is streamed to the connected computer, where they are analyzed further. The FPGA instruments should be modified and recompiled to include the peak finding mechanism directly on the measurement board. This will increase the possible streaming rate and enable modification of the frequency bin number, which is limited to 4096 in the current state.

The bin number defines the frequency (and thus velocity) bin resolution. With 4096 bins, the velocity resolution amounts to 0.01 m/s, which is unnecessarily well defined for the applications in question. Using 1024 or 512 bins would decrease the resolution to a still acceptable level of ~ 0.1 m/s, but enable a higher number of averages at the same streaming rate.

-
- [1] C. Weitkamp, ed., *Lidar: range-resolved optical remote sensing of the atmosphere*, Springer series in optical sciences No. 102 (Springer, New York, 2005).
- [2] C. Slinger, M. Harris, N. Power, T. O. Barns, F. Farm, and N. L. Hr, Introduction to continuous-wave Doppler lidar, Proc. Summer School in Remote Sensing for Wind Energy , 1 (2012).
- [3] N. Vasiljević, M. Harris, A. Pedersen, G. Thorsen, M. Rassmussen, C. Pedersen, P. Hansen, M. Pitter, J. Harris, K. Bajpai, and M. Courtney, Wind measurements with drone-based wind lidars (2019).
- [4] N. Vasiljević, M. Harris, A. Tegtmeier Pedersen, G. Røllighed Thorsen, M. Pitter, J. Harris, K. Bajpai, and M. Courtney, Wind sensing with drone-mounted wind lidars: Proof of concept, Atmospheric Measurement Techniques **13**, 521 (2020).
- [5] A. T. Pedersen, B. F. Montes, J. E. Pedersen, M. Harris, and T. Mikkelsen, Demonstration of short-range wind lidar in a high-performance wind tunnel, European Wind Energy Conference and Exhibition 2012, EWEC 2012 **3**, 1397 (2012).
- [6] P. Hulsman, P. Vlaho, M. Wosnik, and M. Kuehn, Wake Deflection Measurement in a Wind Tunnel with a Lidar WindScanner (2019).
- [7] P. Hulsman, M. Wosnik, V. Petrović, M. Hölling, and M. Kühn, Turbine Wake Deflection Measurement in a Wind Tunnel with a Lidar WindScanner, Journal of Physics: Conference Series **1452**, 10.1088/1742-6596/1452/1/012007 (2020).
- [8] M. Floris Van Dooren, F. Campagnolo, M. Sjöholm, N. Angelou, T. Mikkelsen, and M. Kühn, Demonstration and uncertainty analysis of synchronised scanning lidar measurements of 2-D velocity fields in a boundary-layer wind tunnel, Wind Energy Science **2**, 329 (2017).
- [9] S. A. Barnhart, *Design and Development of a Coherent Detection Rayleigh Doppler Lidar System for Use as an Alternative Velocimetry Technique in Wind Tunnels*, Ph.D. thesis (2020).
- [10] A. Pena, C. B. Hasager, M. Badger, R. J. Barthelmie, F. Bingöl, J. P. Cariou, S. Emeis, S. T. Frandsen, M. Harris, I. Karagali, S. E. Larsen, J. Mann, T. Mikkelsen, M. Pitter, S. Pryor, A. Sathe, D. Schlipf, C. Slinger, and R. Wagner, *Remote Sensing for Wind Energy*, Technical report DTU Wind Energy-E-Report-0084 (EN) (Technical university of Denmark, 2015).
- [11] C. Muñoz-Porcar, Analysis and design of an edge-technique-based Doppler wind lidar . Practical assessment of a laboratory prototype, (2012).
- [12] S. Kapp, Lidar-based reconstruction of wind fields and application for wind turbine control, , 171 (2017).
- [13] S. Oertel, M. Eggert, C. Gutsmuths, P. Wilhelm, H. Müller, and H. Többen, Validation of three-component wind lidar sensor for traceable highly resolved wind vector measurements, Journal of Sensors and Sensor Systems **8**, 9 (2019).
- [14] M. Raffel, C. E. Willert, F. Scarano, C. J. Kähler, S. T. Wereley, and J. Kompenhans, *Particle Image Velocimetry: A Practical Guide*, 3rd ed. (Springer, 2018) p. 668.
- [15] A. Melling, Tracer particles and seeding for particle image velocimetry, Measurement Science and Technology **8**, 1406 (1997).
- [16] G. N. Plass, Mie Scattering and Absorption Cross Sections for Absorbing Particles, Applied Optics **5**, 279 (1966).
- [17] G. de Leeuw and C. W. Lamberts, Influence of refractive index and particle size interval on mie calculated backscatter and extinction, Journal of Aerosol Science **18**, 131 (1987).
- [18] J. A. Stone, Uncalibrated Helium-Neon Lasers in Length Metrology, NCSLI Measure **4**, 52 (2009).
- [19] P. E. Ciddor, Refractive index of air: new equations for the visible and near infrared, Applied Optics **35**, 1566 (1996).
- [20] M. Harris, G. Constant, and C. Ward, Continuous-wave bistatic laser Doppler wind sensor, Applied Optics **40**, 1501 (2001).
- [21] RedPitaya, Red Pitaya - Swiss Army Knife For Engineers.
- [22] Koheron, laser-development-kit (2021).
- [23] N. Angelou, F. F. Abari, J. Mann, T. Mikkelsen, and M. Sjöholm, Challenges in noise removal from Doppler spectra acquired by a continuous-wave lidar, 26th International Laser Radar Conference , 4 (2012).
- [24] S. Fayed, *OPTIMIZATION OF WIND ESTIMATION BASED ON COHERENT LIDAR DATA OPTIMIZATION*, Master thesis engineering physics, Carl von Ossietzky University Oldenburg (2014).